

# Chemical and Topographical Changes upon Sub-100-nm Laser-Induced Periodic Surface Structure Formation on Titanium Alloy: The Influence of Laser Pulse Repetition Rate and Number of Over-Scans

Kai Müller, Francesca Mirabella, Xenia Knigge, Marek Mezera, Matthias Weise, Mario Sahre, Karsten Wasmuth, Heike Voss, Andreas Hertwig, Jörg Krüger, Jörg Radnik, Vasile-Dan Hodoroaba, and Jörn Bonse\*

Titanium and its alloys are known to allow the straightforward laser-based manufacturing of ordered surface nanostructures, so-called high spatial frequency laser-induced periodic surface structures (HSFL). These structures exhibit sub-100 nm spatial periods – far below the optical diffraction limit. The resulting surface functionalities are usually enabled by both, topographic and chemical alterations of the nanostructured surfaces. For exploring these effects, multi-method characterizations were performed here for HSFL processed on Ti–6Al–4V alloy upon irradiation with near-infrared ps-laser pulses (1030 nm,  $\approx 1$  ps pulse duration, 1–400 kHz) under different laser scan processing conditions, i.e., by systematically varying the pulse repetition frequency and the number of laser irradiation passes. The sample characterization involved morphological and topographical investigations by scanning electron microscopy (SEM), atomic force microscopy (AFM), tactile stylus profilometry, as well as near-surface chemical analyses hard X-ray photoelectron spectroscopy (HAXPES) and depth-profiling time-of-flight secondary ion mass spectrometry (ToF-SIMS). This provides a quantification of the laser ablation depth, the geometrical HSFL characteristics and enables new insights into the depth extent and the nature of the non-ablative laser-induced near-surface oxidation accompanying these nanostructures. This allows to answer the questions how the processing of HSFL can be industrially scaled up, and whether the latter is limited by heat-accumulation effects.

## 1. Introduction

Laser-induced periodic surface structures (LIPSS) are a common phenomenon that typically accompany the laser processing of solid materials by linearly polarized laser radiation.<sup>[1–4]</sup> LIPSS can be fabricated on almost all types of materials (metals, semiconductors, dielectrics). These surface structures are generated in a “self-ordered” way within the focal spot of the linearly polarized laser radiation and represent a periodic modulation of the surface topography in the form of a more or less regular grating. Based on their spatial period  $\Lambda$  in relation to the laser wavelength  $\lambda$ , LIPSS are divided into two main groups: *low-spatial frequency LIPSS* (LSFL) with spatial periods  $\Lambda > \lambda/2$  and *high-spatial frequency LIPSS* (HSFL) with spatial periods  $\Lambda < \lambda/2$ . The HSFL were observed solely for the laser processing with ultra-short laser pulses.


LIPSS enable a large variety of different surface functionalizations for applications in the fields of optics, fluidics, tribology, or medicine.<sup>[5–10]</sup> Particularly, the small-scale HSFL provide an appealing, robust,

and straightforward way for surface nanostructuring featuring spatial periods even below 100 nm<sup>[4]</sup> without the need of cost- or time-intensive lithographic or vacuum technologies.

For the HSFL, two types are distinguished with respect to their depth-to-period aspect ratio  $A$  and empirically classified according to the order of their description in the scientific literature as type I or type II.<sup>[2]</sup> HSFL-I with a spatial period of a few hundreds of nanometers only and an aspect ratio  $A > 1$  were reported first during the 1990s on polymer surfaces and on other dielectrics.<sup>[11,12]</sup> Their origin is widely clarified already,<sup>[13]</sup> and can be associated with collective near-field scattering of laser-excited defect centers distributed across the irradiated surfaces along with intra-pulse optical interference and inter-pulse feedback.

K. Müller, F. Mirabella, X. Knigge, M. Mezera, M. Weise, M. Sahre, K. Wasmuth, H. Voss, A. Hertwig, J. Krüger, J. Radnik, V.-D. Hodoroaba, J. Bonse

Bundesanstalt für Materialforschung und -prüfung (BAM)  
Unter den Eichen 87, D-12205 Berlin, Germany  
E-mail: joern.bonse@bam.de

 The ORCID identification number(s) for the author(s) of this article can be found under <https://doi.org/10.1002/pssa.202300719>.

© 2023 The Authors. physica status solidi (a) applications and materials science published by Wiley-VCH GmbH. This is an open access article under the terms of the Creative Commons Attribution License, which permits use, distribution and reproduction in any medium, provided the original work is properly cited.

DOI: 10.1002/pssa.202300719

Titanium and titanium alloys were among the first materials where HSFL-II with  $A \ll 1$  were observed upon fs-laser processing.<sup>[14,15]</sup> It was speculated that the laser-induced oxidation may play an important role on the formation of HSFL on titanium-based materials.<sup>[15,16]</sup> Later, the presence of fs-laser-induced oxidation at the surface of HSFL-II on titanium was proven by micro-Raman Spectroscopy ( $\mu$ -RS), X-ray photoelectron spectroscopy (XPS), and depth-profiling Auger electron microscopy.<sup>[17]</sup>

HSFL-II were reported also on other metals such as nickel,<sup>[18]</sup> and tungsten.<sup>[19]</sup> For tungsten it was demonstrated by directly comparing HSFL-II formed in air and in vacuum environment that the laser-induced oxidation is accompanying the HSFL-II formation but does not cause it.<sup>[19]</sup> This is in line with the recent study of Rudenko et al.<sup>[20]</sup> where the HSFL-II formation for nickel was convincingly attributed to a complex interplay of electromagnetic scattering and hydrodynamic matter-reorganization effects acting on the laser-induced thin melt layer.

Regardless of the exact formation mechanism of the nanostructures, it is evident that, upon laser-processing in air, a superficial laser-induced oxidation layer manifests at the surface of the widely used titanium-based materials.<sup>[17]</sup> However, the question remained open how do the most common laser-processing strategies affect the superficial oxidation? This is relevant, for example, when reducing the overall processing time by using higher laser pulse repetition rates ( $f$ ), or when treating the surface repeatedly with a certain number of identical passes (over-scans, OS). In other words, is the processing of HSFL-II on titanium affected by heat-accumulation effects and how strong does the number of over-scans affect the laser-induced surface oxidation?

In this work, we address these questions. For that, ultrashort laser pulses were used to generate HSFL on polished titanium alloy (Ti–6Al–4V) surfaces under different laser and scan processing conditions. The morphology, its topography and the chemistry of the processed surfaces were characterized via scanning electron microscopy (SEM), atomic force microscopy (AFM), stylus profilometry, time-of-flight secondary ion mass spectrometry (ToF-SIMS), X-ray photoelectron spectroscopy (XPS), and hard X-ray photoelectron spectroscopy (HAXPES). This multi-method approach is utilized to answer the questions how the processing of HSFL can be industrially scaled up, and whether the processing is limited by heat-accumulation effects.

## 2. Experimental Section

The following three sub-sections describe the preparation of the samples, the ps-laser processing and the methods employed for the subsequent surface characterization.

### 2.1. Sample Preparation and Initial Characterization

Rods made of titanium grade 5 (Ti–6Al–4V alloy) were purchased from Schumacher Titan GmbH (Solingen, Germany). The rods were cut to cylinders of 8 mm height and dressed to 24 mm diameter. The top surface of the cylinders was mechanically polished to a mirror-like surface finish with an average surface roughness parameter  $R_a < 10$  nm. The final polishing step was conducted in a colloidal silica suspension (grain size 0.04  $\mu$ m) for fine polishing with an admixture of a small amount of

hydrogen peroxide and nitric acid. Since the samples were processed and stored in ambient air, they exhibit a native oxide layer covering the bulk titanium alloy. Its thickness typically accounts from 4 to 10 nm at the polished sample surfaces.<sup>[21–23]</sup>

### 2.2. Laser Processing

The surface processing of the samples was performed with an industrial thin-disk laser system (TRUMPF, TruMicro 5050 femto edition, Germany) emitting ultrashort laser pulses of 925 fs duration at a center wavelength of 1030 nm and at pulse repetition rates up to 400 kHz. The laser beam was directed to a Galvanometer scanner (ScanLab HurrySCAN II 14, Puchheim, Germany) coupled with an F-Theta focusing lens of 160 mm focal distance. Laser pulse energies were measured by a detector placed after the focusing lens. The focused laser beam was scanned across  $2 \times 2$  mm<sup>2</sup> sized sample areas in a meandering way, i.e., line-wise bidirectional with a line separation (pitch) of  $\Delta y = 5$   $\mu$ m. The scanning direction was always perpendicular to the linear laser beam polarization. The Gaussian beam diameter at the sample surface was determined according to the method of Liu<sup>[24]</sup> as  $2w_0 = 35.5$   $\mu$ m. The peak fluence was calculated from the single pulse energy  $E_p$  via  $\phi_0 = 2E_p/(\pi w_0^2)$ . The number of effective laser pulses per beam spot diameter (in one over-scan) was calculated according to  $N_{\text{eff}} = 2w_0 f/v$ , with  $v$  being the scanning velocity.<sup>[25]</sup> When changing the pulse repetition rate  $f$ , a corresponding adjustment of the scanning velocity  $v$  allowed keeping  $N_{\text{eff}}$  constant during the laser processing.

The values of  $\phi_0$  and  $N_{\text{eff}}$  were optimized and fixed to a set of values ( $\phi_0 = 0.26$  J cm<sup>-2</sup> and  $N_{\text{eff}} = 30$ ) that allowed to generate homogeneous HSFL-II on the polished Ti–6Al–4V surfaces, while processing either at  $f = 1$  kHz or at  $f = 400$  kHz, both for OS = 1 over-scan or for a sequence of OS = 4 over-scans. Since the scanning velocity  $v$  was varied to compensate for the two different pulse repetition rates  $f$ , the laser-processing time for executing a single over-scan (OS = 1) on a  $2 \times 2$  mm<sup>2</sup> area at  $f = 1$  kHz accounted to  $\approx 12$  min, while at  $f = 400$  kHz it took less than 2 s. Multiple over-scans (OS = 4) were executed consecutively, i.e., without any additional delay time between the individual over-scan sequences. Two identical sample copies were laser-processed in a row at the same day, each of it containing a full set of the four different surface areas processed under the mentioned conditions.

**Table 1** presents an overview of the processing parameters for the four different surface areas (A, B, C, D) analyzed within this work. With our approach,  $f$  and OS were systematically varied,

**Table 1.** List of surface areas and the corresponding laser-processing parameters  $f$  (laser pulse repetition rate) and OS (number of over-scans). All other laser-processing parameters were kept constant: peak fluence  $\phi_0 = 0.26$  J cm<sup>-2</sup>, number of effective laser pulses  $N_{\text{eff}} = 30$ , beam diameter  $2w_0 = 35.5$   $\mu$ m, and line separation  $\Delta y = 5$   $\mu$ m.

Sample name	Repetition rate $f$ [kHz]	Number of over-scans OS	Scan velocity $v$ [mm s <sup>-1</sup> ]
A	1	1	1.17
B	1	4	1.17
C	400	1	466.67
D	400	4	466.67

while simultaneously keeping  $\phi_0$ ,  $N_{\text{eff}}$ ,  $2w_0$ , and  $\Delta\gamma$  constant. After the laser processing, the samples were cleaned for 5 min in an ultrasonic bath in acetone and subsequently stored in a desiccator.

### 2.3. Surface Analytics

SEM and atomic force microscopy (AFM) were performed to characterize the surface morphology and to quantify the dimensions of the laser-generated surface structures. To avoid interference with other methods, SEM and AFM imaging was done on one of the sample copies. Chemical surface analyses were conducted on the second identical sample copy by means of ToF-SIMS and by simultaneously performed XPS and HAXPES.

For SEM characterization of the surface morphology, a Zeiss Supra 40 (Oberkochen, Germany) microscope was operated in InLens mode using an electron acceleration voltage of 10 kV. All samples were investigated without being necessary to coat the surface to ensure a good conductivity. To improve contrasts and remove organic residue from the surface, plasma cleaning was employed in-situ (Downstream Asher GV10 $\times$ , ibss Group Inc., Burlingame, USA; 5 min, 75 W, ambient air). The public domain software *ImageJ* (Version 1.54, National Institutes of Health, Bethesda, USA)<sup>[26]</sup> was used for quantifying distances and dimensions from SEM micrographs.

For AFM analyses of the surface topography, a Digital Instruments Dimension 3100 (Santa Barbara, USA) was employed in tapping mode. For this silicon cantilever probes ( $n^+$ -silicon, PointProbe NCH, Nanosensors) featuring a nominal tip radius of 10 nm were used at ambient conditions. The corresponding images of  $2 \times 2 \mu\text{m}^2$  containing  $512 \times 256$  lines in  $x$ - and  $y$ -direction were measured with a nominal resolution of 20 pm in  $z$ -direction ( $1.3 \mu\text{m}/16$  bit in full  $z$ -scale). All image data are displayed as two-dimensional color maps of the surface topography, using a color scale for visualizing the topographic height ( $z$ -) variations.

Spatial periods of the LIPSS were determined according to a procedure described in a previous work<sup>[27]</sup> using the free software *Gwyddion* (Version 2.53, Czech Metrology Institute, Brno, Czech Republic).<sup>[28]</sup> The procedure is the same for SEM and AFM data, with exception of AFM images having a quadratic size of  $2 \mu\text{m}$ . The procedure will, therefore, be described for SEM only. In short, SEM images were taken at a  $100\,000\times$  nominal magnification and cut to a quadratic size of  $2.6 \mu\text{m}$  side length. Subsequently, the two-dimensional Fast Fourier Transformation (2D-FFT) was performed using default parameters (output type: modulus; windowing type: Hann; “Subtract mean value beforehand”). The output type “modulus” provides absolute value of the complex Fourier coefficient. The windowing type “Hann” selects the mathematical Hanning weighting function  $w_{\text{Hann}}(x) = 0.5 + 0.5 \cdot \cos(2 \cdot \pi \cdot x)$ , with the independent variable  $x \in [0, 1]$  corresponding to the normalized window coordinates, to suppress the data at the edges of the image.<sup>[29]</sup>

The profiles along the main axis were then taken and Lorentzian fits were performed on the first, left ( $k_l$ ), and right peak ( $k_r$ ) of the main peak. The mean spatial period  $\Lambda$  was calculated using the following formula:  $\Lambda = 2/(k_r - k_l)$ . The uncertainties for  $\Lambda$  were calculated here using the

Gaussian error propagation of uncertainty taking into account the error given by *Gwyddion* as the error for the peak positions.

A Bruker DektakXT stylus profilometer was used to measure topographic features in a tactile way with high vertical resolution (nominal resolution  $\approx 1$  nm), with a stylus tip radius of  $2.5 \mu\text{m}$  and a cone angle of  $45^\circ$ . Data were acquired after calibration against a certified VLSI step height reference sample, using a total of 10 lines perpendicular to the laser-processed pattern, spanning over about 2–3 mm. A lateral resolution of  $1 \mu\text{m}/\text{point}$  and draw speed of  $10 \mu\text{m s}^{-1}$  were used for the measurement. To avoid overfitting of data while reducing the effect of sample curvature, mean plane subtraction was performed in *Gwyddion* using standard parameters.

The chemical composition of the laser-processed and the non-irradiated (polished) Ti substrates was analyzed using ToF-SIMS. In combination with additional ion sputtering, depth-profiles of the near-surface sample composition can be measured. ToF-SIMS was performed on a TOF-SIMS IV instrument (ION-TOF GmbH, Münster, Germany). This spectrometer was equipped with a Bi cluster primary ion source and a reflectron-type time-of-flight analyzer. Ultra-high vacuum (UHV) base pressure was  $< 10^{-8}$  mbar. For high mass resolution, the Bi source was operated in “high current bunched” mode providing short Bi primary ion pulses at 25 keV energy. The short pulse length of 1 ns duration allowed for high mass resolution and unambiguous chemical assignments. For high lateral resolution, the source was operated in a non-bunched mode (bust alignment) to avoid chromatic aberration. For depth-profiling, a dual beam analysis was performed in interlaced mode: The primary ion source was again operated in the non-bunched mode with a scanned area of  $150 \times 150 \mu\text{m}^2$  ( $128 \times 128$  data points) and a sputter gun (operated with Cs ions, 3 keV, scanned over a concentric field of  $300 \times 300 \mu\text{m}^2$ , target current 150 nA) was applied to erode the sample. As sputtered titanium surfaces were exceptionally good getter substances for oxygen from the residual gases in the UHV system, data acquisition was performed at pressures below  $5 \times 10^{-9}$  mbar and a constant background count rate was corrected for. All signals were recorded as a function of the Cs ion sputter time. In order to obtain from the sputtering time-profile a depth-resolved profile of the analytical ions, the Cs ion sputter rate must be determined. This was performed by tactile stylus profilometric measurements quantifying the sputter crater depth at the end of the corresponding depth-profiles in the Ti-6Al-4V samples (data now shown here for brevity). Since the Cs ion sputter rate may additionally depend on the material, a physical vapor deposition-coated  $\text{TiO}_2$ -layer of known thickness (200 nm as determined by VASE) deposited on a silicon wafer was used as a second material reference. Average Cs sputter rates of 0.116 and 0.188  $\text{nm s}^{-1}$  were obtained for Ti-6Al-4V and  $\text{TiO}_2$ , respectively. The sharp interface between the  $\text{TiO}_2$ -layer and the silicon wafer of the second material reference sample allowed additionally an estimate of the depth-resolution to be performed, i.e., a value below 10 nm here. All ToF-SIMS depth-profiles display the measurements versus the sputter time (bottom axis) and are additionally complemented with depth information (top axis) estimated with the sputter rate of  $0.188 \text{ nm s}^{-1}$ .

X-ray photoelectron spectroscopy (XPS and HAXPES) was performed with an ULVAC-PHI (Minnesota, USA) “Quantes”

lab-based spectrometer that is equipped with a monochromatic Al K $\alpha$  source at 1486.6 eV for XPS and with a monochromatic Cr K $\alpha$  source at 5414.8 eV for HAXPES. As the same electron optics is used for both methods it was possible to measure at the exact same spot position at the sample surface. From high-resolution spectra it is possible to assess the surface chemistry of the probed sample locations. An area of  $\approx 100 \times 100 \mu\text{m}^2$  was analyzed. Photoelectrons were collected at an emission angle of 45°. The time per step was 50 ms. The pressure in the sample chamber was controlled and smaller than  $10^{-6}$  Pa during the measurement. Survey spectra for an overview of the elemental composition were acquired at 280 eV pass energy and an energy step size of 1 eV for photoemission energies between 0 and 1200 eV (XPS) or 5000 eV (HAXPES), while high-resolution spectra were recorded at 55 eV pass energy and 0.1 eV energy step size for XPS and 69 eV pass energy and 0.125 eV step size for HAXPES. The X-ray source settings were 25 W and 15 kV for XPS measurements and 50 W and 20 kV for HAXPES measurements. To get a better signal-to-noise ratio, measurements were repeated in multiple cycles. The carbon C 1s peak at 285.0 eV was used as internal reference. Experimental differences in this peak energy due to charging of the surface during the measurements were used for a correction (shift) of the binding energies of all other lines. The experimental uncertainty of the binding energy in both the XPS and HAXPES measurements was below 0.4 eV. For the specified conditions, the information depth for the XPS accounts to  $\approx 10$  nm, while for the HAXPES mode is  $\approx 30$  nm.

### 3. Results and Discussion

#### 3.1. Surface Morphology and Topography

The surface morphology and topography were analyzed by various methods, including SEM (Section 3.1.1) and AFM (Section 3.1.2). This allows the nanoscale geometrical characterization of the HSFL-II formed on Ti-6Al-4V for the chosen laser processing approaches.

##### 3.1.1. Scanning Electron Microscopy (SEM)

Due to the small feature size of HSFL that is surpassing the optical diffraction limit, optical microscopy is not a feasible method to image the laser processed surfaces. Hence, SEM was used, which allows for higher magnifications and, visualization of structures of a few nm. **Figure 1** displays high-resolution SEM images of all four HSFL acquired at the same magnification. Surface structures processed with one over-scan (OS = 1, left column) appear flat and uniformly textured (A, C). The structures treated with four over-scans (OS = 4, right column) exhibit shorter ridges and fraying of ends (B, D). Manual analysis reveals larger feature sizes and irregularity at the structure processed at 400 kHz and OS = 4 (D) compared to 1 kHz and OS = 4 (B). This is not as visibly pronounced for the structures processed with only one over-scan when comparing the sample areas A and C. However, large differences in the HSFL regularity can be seen

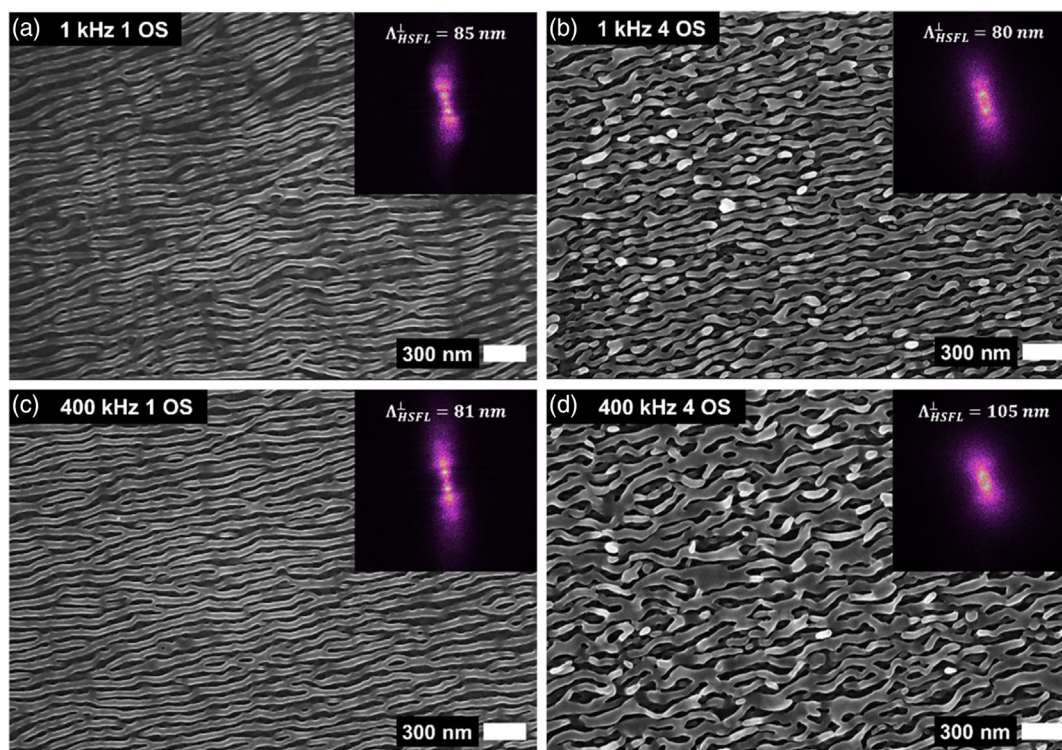


**Figure 1.** Top-view SEM micrographs of ps-laser-generated HSFL on Ti-6Al-4V titanium alloy processed with two different pulse repetition rates (rows) and with two different numbers of over-scans (columns). a) sample area processed with 1 kHz and one over-scan (A), b) 1 kHz and four over-scans (B), c) 400 kHz and one over-scan (C), d) 400 kHz and four over-scans (D). The insets display 2D-FFTs of the corresponding micrographs.

when comparing the left and the right column of Figure 1, i.e., between one and four over-scans.

The SEM images were further evaluated by performing two-dimensional Fourier transforms (2D-FFTs), as displayed as insets in the upper-right corners of the corresponding micrographs. The *ImageJ* software was used to manually measure the average HSFL ridge width of all structures (appearing as bright ridges between dark grooves in the micrographs) at ten different points, as well as to calculate the average HSFL period (length between beginning of one ridge to the beginning of a neighboring ridge) from the 2D-FFTs. The average ridge width ( $w_{\text{HSFL}}$ ) of all structures is very similar (44–51 nm), see **Table 2**. Increasing the number of over-scans OS influences the standard deviation of the ridge width, as thinner and wider ridges appear. The average HSFL period values cover a wider range between 80 and 105 nm (Table 2). Thus, the HSFL period is about twice the HSFL ridge width, and all values do not deviate by more than  $\approx 20\%$  here. The irregularity of the HSFL varies significantly between one and four over-scans.

### 3.1.2. Atomic Force Microscopy (AFM)

AFM was performed on  $2 \times 2 \mu\text{m}^2$  sized areas in order to quantify the depth variations associated with the HSFL-II on Ti–6Al–4V titanium alloy. **Figure 2** shows again the representative areas of each HSFL processing case (A–D). The micrographs show great resemblance to the micrographs taken by SEM, i.e., apparent flat surface for areas processed with one over-scan (A, C), while areas processed with four over-scans (B, D) exhibit increased irregularity. The latter two micrographs (B, D) also indicate a characteristic tip-artefact arising from an altered tip-sample-contact geometry that may explain the differences to the corresponding SEM micrographs previously shown in Figure 1. Note that for such conditions, the AFM tip may not reach the bottom of the HSFL valley. Thus, for the AFM surface topographies B and D, the average HSFL modulation depth may be underestimated and can only serve as a lower limit here.

**Table 2.** Geometrical characteristics of HSFL-II and corresponding oxide layer thickness, as measured by SEM, AFM, stylus profilometry, and ToF-SIMS on the four ps-laser-processed Ti–6Al–4V surface areas A–D.

Sample area	A	B	C	D
Average ridge width (SEM)	$50 \pm 5$	$47 \pm 7$	$44 \pm 5$	$51 \pm 9$
$w_{\text{HSFL}}$ [nm]				
Average spatial period (SEM)	$85 \pm 1$	$80 \pm 1$	$81 \pm 1$	$105 \pm 2$
$\Lambda_{\text{HSFL}}$ [nm]				
Average spatial period (AFM)	$84 \pm 1$	$96 \pm 1$	$81 \pm 1$	$93 \pm 1$
$\Lambda_{\text{HSFL}}$ [nm]				
Average modulation depth (AFM)	$27 \pm 2$	$\geq 44 \pm 3$	$37 \pm 3$	$\geq 49 \pm 5$
$h_{\text{HSFL}}$ [nm]				
Mean surface height change (Stylus)	12	48	27	67
$\Delta z$ [nm]				
Mean oxide layer thickness (ToF-SIMS)	21	52	24	92
$d_{\text{ox,mean}}$ [nm]				

As for SEM, significant differences between the areas processed at different laser pulse repetition rates cannot be detected by AFM, indicating that thermal heat-accumulation is not present in HSFL processing for repetition rates up to 400 kHz. From area A it can be inferred that for our processing conditions the HSFL are not affected by the underlying grain structure of the alloy, i.e., the nanostructures can be homogeneously “written” onto the polished metallic surfaces, allowing for a large-area upscaling for potential practical applications.

In analogy to the SEM analyses, the average spatial periods  $\Lambda_{\text{HSFL}}$  were evaluated on basis of the AFM micrographs. The results are also compiled in Table 2 along with the AFM-derived structure height, referred to as HSFL modulation depth ( $h_{\text{HSFL}}$ ) in the following. For calculating  $h_{\text{HSFL}}$ , the maximum peak-to-valley height of neighbored HSFL ridges was evaluated and averaged over a cross-sectional line range of  $2 \mu\text{m}$  at five different spatial positions.

The average spatial periods for areas processed using one over-scan ( $\text{OS} = 1$ ) is very similar between AFM and SEM, while the values for four over-scans ( $\text{OS} = 4$ ) differ by  $\approx 10\%$  between the techniques. The value for the average HSFL modulation depth  $h_{\text{HSFL}}$  varies between 27 nm (sample area A) and 49 nm (sample area D). Nevertheless, there is a clear trend that the modulation depth of HSFL is larger for areas processed at four over-scans compared to areas processed with a single over-scan only.

One question left open so far is whether the laser processing of HSFL-II on Ti–6Al–4V has an ablative or additive effect, i.e., if there is a global depression or a protrusion in the areas where the sample was laser-treated? This question could, undoubtedly, not be answered previously by using white light interference microscopy (WLIM) as the presence of a possibly transparent and very thin oxide layer (of  $< \lambda/2$  thickness) may not be properly resolved. To avoid this disadvantage of optical techniques, mechanical stylus profilometry was chosen as a complimentary contact-based method allowing additionally to inspect larger areas than accessible by AFM. For brevity, the results are summarized only here: The stylus profilometric measurements were recorded across the entire laser processed areas. The mean change of the height of the surface ( $\Delta z$ ) was evaluated at the edges of all four HSFL-processed areas. Our stylus profilometry indicated step-like elevated surface levels in regions where HSFL were formed, i.e., the laser processing occurs “additively” and generates a shallow surface protrusion. Such laser-induced surface swelling effects were already observed for the multi-pulse irradiation of oxidation-prone titanium nitride<sup>[30]</sup> and for single-pulse irradiation of aluminum by ultrashort laser pulses.<sup>[31]</sup> The corresponding height changes are listed in Table 2 and account to  $\Delta z = 12$  nm (A), 48 nm (B), 27 nm (C), and 67 nm (D). These observations point towards a laser-induced oxidation process at the treated titanium alloy surfaces as most titanium oxides exhibit a reduced mass density compared to the pure metal [ $\rho(\text{Ti}) = 4.52 \text{ g cm}^{-3}$ ,  $\rho(\text{TiO}_2, \text{ rutile}) = 4.23 \text{ g cm}^{-3}$ ,  $\rho(\text{Ti}_2\text{O}_3) = 4.49 \text{ g cm}^{-3}$ , see ref. [32]]. In such a non-ablative processing regime, the reduced mass density imposes an increased specific volume of the near-surface material manifesting as a surface protrusion then.<sup>[30]</sup> Additionally, sub-surface nanovoids may form upon ultrashort pulsed laser-induced irradiation of metals,<sup>[33]</sup> an effect that may also contribute to the surface swelling here.

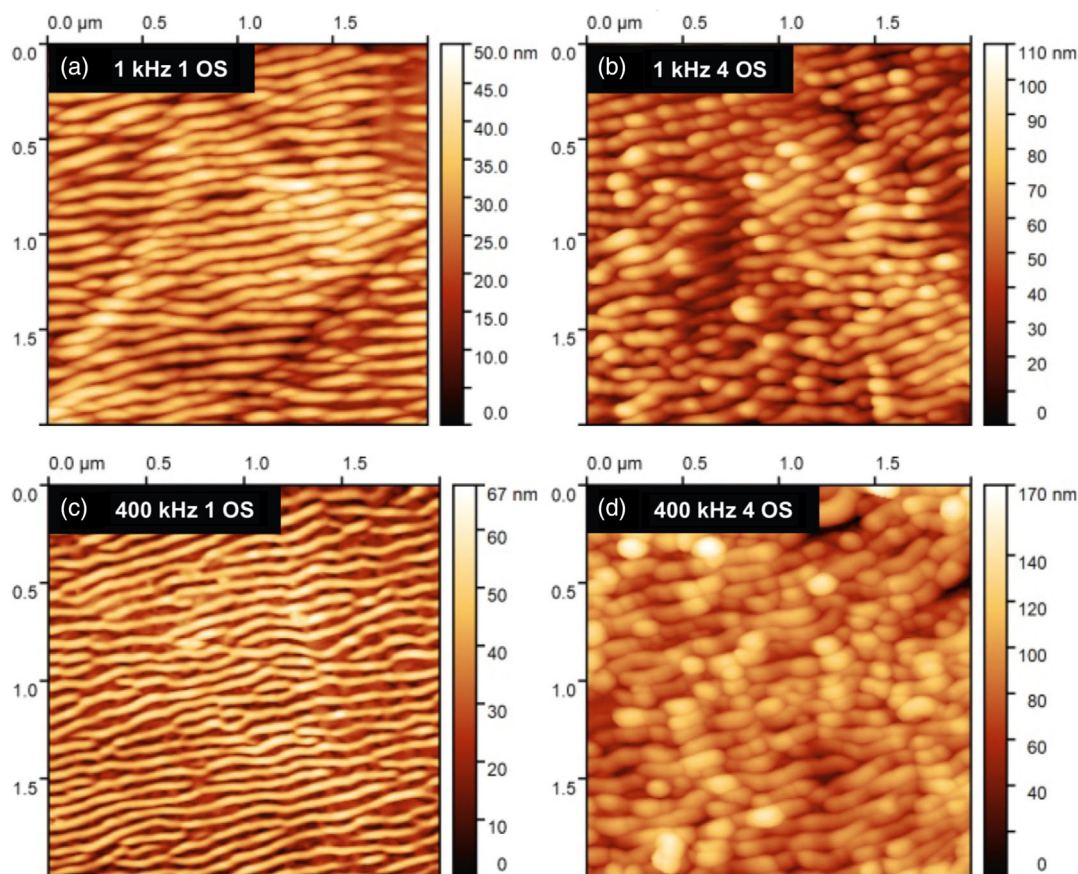


**Figure 2.** AFM surface topographies for the four ps-laser-generated HSFL (A–D). Processing conditions are described in Figure 1 and Table 1: a) A, b) B, c) C, and d) D. Note the individually different z-scale (color) ranges.

In summary, generally a good agreement between SEM and AFM spatial periods is found. The HSFL periods  $\Lambda_{\text{HSFL}}$  are widely unaffected by the laser pulse repetition rates. In contrast, the number of over-scans (OS) moderately increases  $\Lambda_{\text{HSFL}}$  and  $h_{\text{HSFL}}$ , while the HSFL ridge length and regularity decrease with OS.

### 3.2. Surface Chemistry

The surface chemistry of the HSFL-covered Ti–6Al–4V samples was studied by different analytical methods. ToF-SIMS was combined with an ion-sputter depth-profiling (Section 3.2.1), tracking specific molecular constituents in the depth of the sample beneath its surface. Complementary XPS and HAXPES allowed to simultaneously probe the presence of specific chemical compounds (metal oxides, intermetallic oxides, metals) at different information depth below the adventitious carbon layer covering the surface (Section 3.2.2).

#### 3.2.1. Time-of-Flight Secondary Ion Mass Spectrometry (ToF-SIMS)

To investigate the elemental and molecular depth distribution of species, ToF-SIMS was used for depth-profiling of the HSFL-covered sample areas A–D as well as for a polished surface

area as a reference (Ref.). **Figure 3** summarizes in each graph (A (a)–D (d)) the corresponding depth-profiles for the two most intense metal oxide ions,  $\text{TiO}^-$  (green curves) and  $\text{AlO}^-$  (purple curves) along with a profile of the  $\text{TiO}^-$  ion recorded for the polished reference (grey curves). For areas processed using one over-scan (OS = 1, A and C)  $\text{AlO}^-$  is the more intense ion, while for four over-scans (OS = 4, B and D)  $\text{TiO}^-$  becomes the more intense ion. Significant signal broadening of the depth-profiles is observed for OS = 4, that is even more pronounced at the 400 kHz processed area. Due to its low yield in negative ion mode, vanadium ions were not evaluated and are not shown here.

The oxide layer thickness  $d_{\text{ox,mean}}$  estimated from a 50% criterion (depth of decay to 50% of the maximum signal) of the  $\text{TiO}^-$  ion signal differs significantly, ranging between  $\approx 21$  nm (1 kHz, OS = 1, sample area A) and  $\approx 92$  nm (400 kHz, OS = 4, sample area D), see Table 2. HSFL processed by one over-scan (OS = 1) shows a titanium oxide layer thickness in the same order of magnitude as the native oxide layer at the polished reference sample area (sample area A – 1 kHz:  $d_{\text{ox,mean}} = 21$  nm; C – 400 kHz: 24 nm; Reference:  $d_{\text{ox,mean}} = 4$  nm). Surfaces repetitively processed 4 times (OS = 4) exhibit a titanium oxide layer thickness at least ten-times as thick as the native oxide layer. The HSFL processed at 400 kHz and OS = 4 (sample area D) even show a titanium

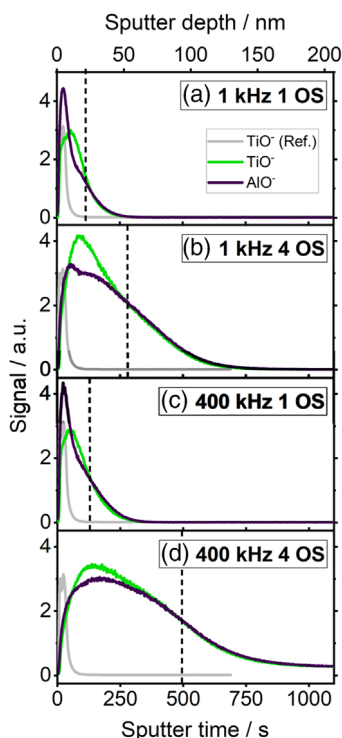


**Figure 3.** ToF-SIMS sputter-depth-profiles of  $\text{TiO}^-$  (green curves) and  $\text{AlO}^-$  ions (purple curves) for sample areas A (a)–D (d) and for the polished reference “Ref.” (grey curves). The dashed vertical lines mark the thickness of the laser-induced oxide layer as deduced from the 50%-criterion.

oxide layer thickness more than twenty-times the one of the polished reference surface, and about 4 to 5 times the value of the 1 kHz and OS = 1 processed HSFL (A).

These findings highlight the strong influence of the number of over-scans OS on the resulting oxide layer thickness at the surface of HSFL-II on Ti-6Al-4V, while the laser pulse repetition rate  $f$  has a rather small influence only for a single over-scan and a moderate influence for four over-scans. The number of over-scans not only influences the oxide layer thickness, but also the ratio of the two main metal oxide ions,  $\text{AlO}^-$  and  $\text{TiO}^-$ . For one over-scan (OS = 1) the  $\text{TiO}^-$  signal is for the outermost layers more intense than the  $\text{AlO}^-$  signal, while for four over-scans (OS = 4) the opposite behavior is observed. One reason is assumed to be due to diffusion during laser-processing, that spreads the aluminum over a wider depth range, while for the less-often processed structures or the polished reference sample it remains localized near the surface.

However, two remarks must be made regarding the depth-profiling ToF-SIMS measurements conducted here. First, a quantification of the chemical surface composition (in at%) is not possible since suitable reference samples are not available. Note that the measured ToF-SIMS signal is the result of an ion yield upon 25 keV Bi-ion probing, which should not be confused with an elemental concentration at the sputtered surface here. The ion yield is not known for the measurement conditions. Therefore, a simple correlation with the elemental concentration is not possible. Only the trend during the

sputtering can be discussed. Second, in ToF-SIMS the influence of *sputter-reduction* processes through the impact of the 3 keV Cs-ion (and also the 25 keV Bi-ion) sputtering cannot be ruled out. This effect could chemically reduce the superficial metal oxides (e.g., converting  $\text{TiO}_2$  into  $\text{Ti}_2\text{O}_3$  or subsequently even into  $\text{TiO}$ )<sup>[34]</sup> and is, thus, potentially affecting the interpretation of the surface analytic results. Therefore, additional beam damage-free measurements probing the sub-surface chemistry at different depths and not relying on ion-sputter depth profiling are desired. A solution can be provided by the combination of XPS and HAXPES when simultaneously probing identical surface areas.

### 3.2.2. X-ray Photoelectron Spectroscopy (XPS and HAXPES)

The spectral analysis of XPS and HAXPES data allows to quantify the elemental composition of the sample surface. **Figure 4** compiles the survey spectra (0–1200 eV) recorded at the four different HSFL-covered surface areas (A–D) along with a measurement at the polished surface area as a reference. The top-part of the figure presents the group of HAXPES spectra, while the bottom part displays the corresponding XPS spectra. Both groups of spectra were scaled individually in their intensity (in a.u.). Moreover, the XPS and HAXPES spectra are vertically shifted for better visibility.

In all survey spectra the elements Ti, O, Al, and C are found to be present at the surface, as well as small amounts of Ca and F. Significant signals of V were not detected. The direct comparison of XPS spectra (representing 10 nm information depth) and HAXPES spectra (representing 30 nm information depth) shows a significant decrease of the amount of C when analyzed with HAXPES, as C is located on the surface of the sample in adsorbed hydrocarbon molecules from the air, so-called adventitious carbon. With both, XPS and HAXPES, a quantification of the surface composition was performed.

**Table 3** compiles the elemental surface composition (at%) as obtained from the corresponding XPS and HAXPES survey spectra for the four different HSFL-covered surface areas (A–D) and for the polished reference (Ref.).

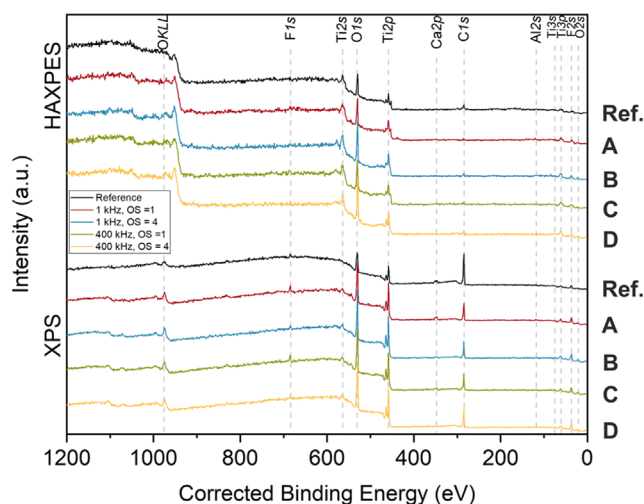


**Figure 4.** Survey spectra (XPS and HAXPES) of corrected binding energies recorded between 0 and 1200 eV at different sample areas (A–D and for the polished reference).

**Table 3.** Elemental surface compositions of four ps-laser processed Ti–6Al–4V surface areas A–D and the polished area (Ref.), as quantified by XPS and HAXPES.

Sample area		A	B	C	D	Ref.
Elemental concentration		[at%]				
XPS	C 1s	39.1	34.4	34.4	39.0	62.8
	O 1s	44.1	47.0	47.5	45.2	27.1
	Ti 2p	14.4	16.0	15.2	13.6	5.9
	Al 2p	2.3	2.7	3.0	2.1	4.3
HAXPES	C 1s	13.2	11.3	12.6	18.8	34.6
	O 1s	43.5	41.2	42.1	47.1	36.8
	Ti 2p	19.7	14.7	17.2	14.2	15.8
	Al 2p	23.7	32.8	28.1	19.9	12.7

To further evaluate the surface chemistry, high-resolution spectra were recorded. The corresponding measurements of Ti, Al, and O are discussed in the following. Here, again the intensity of the HAXPES signals was adjusted to be comparable to that of the XPS measurements.

**Figure 5** presents high-resolution XPS and HAXPES spectra of the Ti 2p doublet transition, recorded between 447.5 and 475 eV at the four different HSFL-covered surface areas A–D and at a polished surface region as a reference. Vertical dashed lines indicate the positions of the peaks of the Ti 2p<sub>1/2</sub> and the Ti 2p<sub>3/2</sub> photoelectron-emission lines of titanium in the Ti<sup>IV</sup> oxidation state at 464.3 and 458.4 eV, respectively. These peaks are characteristic for titanium dioxide TiO<sub>2</sub>. Additionally, the position of the Ti 2p<sub>3/2</sub> peak of metallic titanium (Ti<sup>0</sup>) and oxidic TiO (Ti<sup>II</sup>) and Ti<sub>2</sub>O<sub>3</sub> (Ti<sup>III</sup>) are indicated at 453.8, 455.4, and 457.4 eV, respectively.<sup>[17]</sup> All five XPS spectra indicate predominantly the presence of TiO<sub>2</sub> at the surface. Only at the polished reference surface a very weak peak of metallic Ti<sup>0</sup> can be observed. The laser-irradiated sample areas (A–D) all exhibit additionally a weak shoulder at 457.4 eV, revealing the (minor)

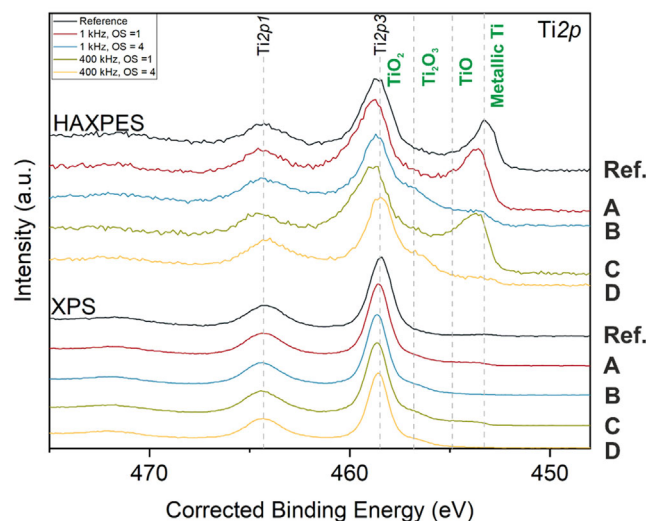


**Figure 5.** High-resolution XPS and HAXPES spectra of the Ti 2p doublet transitions at different sample areas (A–D and for the polished reference).

presence of Ti<sub>2</sub>O<sub>3</sub>. The latter species was reported already for fs-laser generated HSFL-II on pure (grade 1) titanium.<sup>[17]</sup> Interestingly, the HAXPES spectra recorded at the sample areas A and C (both OS = 1) and at the polished surface exhibit very pronounced peaks of metallic Ti<sup>0</sup> and oxidic Ti<sup>IV</sup>. Again, a weak shoulder related to Ti<sub>2</sub>O<sub>3</sub> (Ti<sup>III</sup>) can be found in all laser-processed surface regions (A–D). However, the Ti<sup>0</sup> peak is significantly decreased in intensity at the corresponding sample areas B and D, i.e., for the samples treated with OS = 4 over-scans.

These observations can be jointly explained as follows: the reference area (Ref.) represents the polished Ti–6Al–4V alloy that is covered by a native oxide layer consisting mainly of amorphous titania. According to the ToF-SIMS measurements presented in Section 3.2.1, its thickness is ≈4 nm here. Since HAXPES exhibits an information depth of ≈30 nm, it can probe the bulk of the Ti-alloy underneath the native oxide layer, resulting in the pronounced peak of metallic Ti at 453.8 eV. In contrast, the information depth of XPS of ≈10 nm only is similar to the thickness of the native oxide layer, resulting in a much weaker signal of the metallic titanium in the reference measurement. For the surface areas processed at a single over-scan (A, C) the same scenario applies, where the ps-laser-induced titanium-containing oxide layer is thicker than the information depth of the XPS but thinner than the information depth of HAXPES. That laser-induced oxide layer consists mainly of TiO<sub>2</sub> with some minor contributions of Ti<sub>2</sub>O<sub>3</sub>. For OS = 4 over-scans (B, D), the thickness of the laser-induced titanium containing oxide layer then starts exceeding the information depth of the HAXPES. These findings are fully in line with the little available literature that, generally, indicates an overall increase of thickness of the surface covering oxide layer upon ultrashort pulse laser-processing in air environment.<sup>[17,23,35]</sup>

**Figure 6a** presents high-resolution XPS/HAXPES spectra of the Al 2p doublet transition, acquired between 67.5 and 83.3 eV at the four different HSFL-covered surface areas A–D and for the polished reference. The two photoemission lines of the metallic Al 2p<sub>1/2</sub> and Al 2p<sub>3/2</sub> transition exhibit differences in the binding energy of less than 1 eV and cannot be resolved here. However, the convoluted Al 2p binding energy is sensitive to the oxidation state and can be used to identify chemical species. The vertical dashed lines in Figure 6a indicate the positions of the Al 2p peaks of aluminum in the Al<sup>III</sup> oxidation state at 73.75 eV and in the Al<sup>0</sup> oxidation state at ≈72 eV, respectively. These peaks are characteristic for aluminum in Al<sub>2</sub>O<sub>3</sub> and for metallic Al.

The XPS spectra indicate solely the presence of Al<sub>2</sub>O<sub>3</sub> at the surface. Note that the dominant Al 2p peak of the polished reference surface exhibits a pronounced shoulder toward higher binding energies (marked by a vertical dashed line) that may arise from aluminum–titanium–oxides (e.g., Al–O–Ti).<sup>[36]</sup> That shoulder widely vanishes with the number of over-scans OS, indicating that the thickness of the laser-induced oxide layer is increased, while the superficial aluminum–titanium–oxides turn into the thermodynamically most stable form Al<sub>2</sub>O<sub>3</sub>. This behavior clearly points toward the laser-induced oxidation of the Al compound at Ti–6Al–4V surfaces during the HSFL formation.

The corresponding HAXPES spectra exhibit a low signal-to-noise ratio, which makes an evaluation difficult here. The Al 2p photo-emission peak of aluminum oxide appears as a wide shoulder. The spectra recorded at the polished reference surface



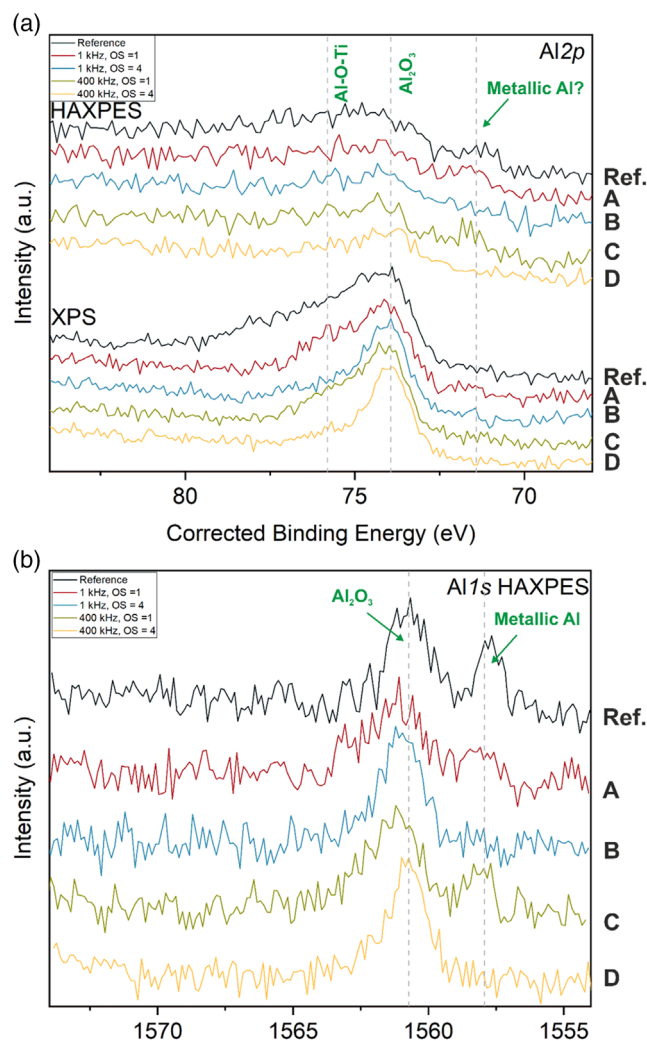


**Figure 6.** a) High-resolution XPS and HAXPES spectra of the Al 2p doublet transitions at different sample areas (A–D and for the polished reference). b) High-resolution HAXPES spectra recorded for the Al 1s singlet transition at the same sample areas.

(Ref.) and with one over-scan (sample areas A and C) may indicate the presence of metallic Al arising from the bulk (position marked by a vertical dashed line), but at the given signal-to-noise ratio, this cannot be safely concluded here.

In contrast to XPS, HAXPES allows the detection of the Al 1s peak with a relatively high sensitivity factor. Figure 6b displays high-resolution Al 1s spectra. The reference spectrum as well as the curves A and C (both related to a single over-scan) show peaks corresponding to Al<sub>2</sub>O<sub>3</sub> (1561 eV) as well as to the metallic Al (1558 eV). The HSFL-covered surfaces processed with OS = 4 over-scans (B, D) do not present the peak of metallic aluminum. Thus, the aluminum-containing oxide layer is much thicker in the latter cases than for surfaces processed with one over-scan. These results further support the above-mentioned scenario.

**Figure 7** compiles the high-resolution XPS and HAXPES spectra of the O 1s singlet transition, recorded between 525 and 539 eV at the four different HSFL-covered surface areas A–D and for the polished reference. The two vertical dashed lines

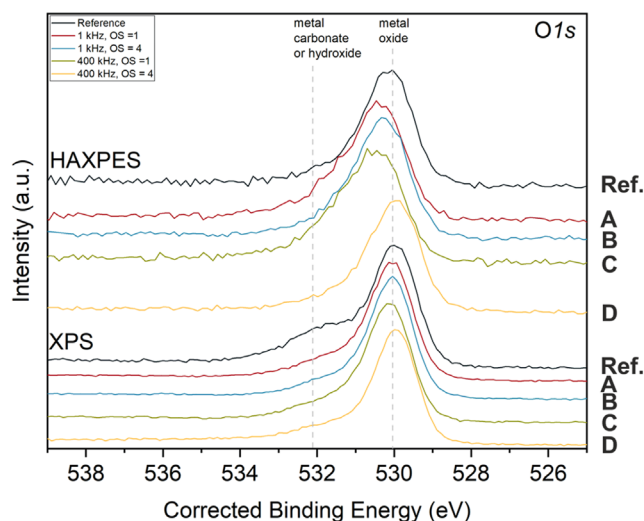


**Figure 7.** High-resolution XPS and HAXPES spectra of the O 1s singlet transitions at different sample areas (A–D and for the polished reference).

indicate the positions of the photoelectron-emission lines of metal oxides ( $\approx 530$  eV) and of metal carbonates or metal hydroxides ( $\approx 532.1$  eV).

In XPS the dominant peak is located at  $\approx 530$  eV for all sample areas, arising from near-surface presence of TiO<sub>2</sub> and Al<sub>2</sub>O<sub>3</sub> proven above. Additionally, the peak shoulder located at 532.1 nm indicates a surface-covering layer containing metal hydroxides and carbonates. In HAXPES these signals largely vanish due to the increased information depth. Simultaneously, the main peak tends to shift by up to 0.5 eV to larger binding energies.

In view of the XPS and HAXPES results previously discussed for Ti and Al, we suggest here that the moderate apparent shift for the curves A, B, C in HAXPES is caused by the formation of a laser-induced sub-surface layer consisting of thermodynamically less stable metal oxides, such as Ti<sub>2</sub>O<sub>3</sub> and TiAl<sub>x</sub>O<sub>y</sub>, with a thickness between 10 and 30 nm. For a large number of over-scans, the thermodynamically most stable TiO<sub>2</sub> and Al<sub>2</sub>O<sub>3</sub> are again the dominant metal oxide over layer thicknesses exceeding the larger information depth of HAXPES (curve D).

Based on the chemical analyses, the following physico-chemical scenario is drawn for the oxidation effects accompanying the HSFL formation on Ti–6Al–4V titanium alloy: the ultrashort pulsed laser radiation is absorbed at the surface by the electronic system of the metal, triggering a plethora of different subsequent energy relaxation processes: already during the laser irradiation, intra-pulse electromagnetic scattering and absorption takes place and is leading via the coupling to hydrodynamic effects and additional inter-pulse feedback to the formation of HSFL-II.<sup>[20,37]</sup> The thermal energy transferred from the optical absorption via electron-phonon relaxation to the lattice involves melting and the heating of a near surface layer, thus increasing the oxidation rates of the highly reactive materials titanium and aluminum in the presence of the ambient air. Given the involved high temperatures that are exceeding the melting temperature of the titanium alloy ( $\approx 1660$  °C), the laser-excited material is driven towards oxidation in the thermodynamically most stable forms of the oxides, i.e., titanium

dioxide  $\text{TiO}_2$  and aluminum oxide  $\text{Al}_2\text{O}_3$ , here. This is facilitated at the sample surface, where the access to the reaction partner oxygen from the ambient air is given. In deeper lying regions underneath the so-called heat-affected zone (HAZ) oxygen diffusion is impeded by the covering material. In the transitional region between the bulk and the surface, less-oxygen-containing constituents can form  $\text{Ti}_2\text{O}_3$ ,  $\text{TiO}$ ,  $\text{Al-O-Ti}$ , or other sub-stoichiometric oxides and intermetallic phases. The beam scanning irradiation with multiple ( $N_{\text{eff}}$ ) laser pulses further reinforces these depth-graded oxidation effects via the repetitive

surface heating and cooling cycles, and through the (inter-pulse) topographic changes of the surface that may also involve material defects, such as nanopores, cracks, vacancies, and interstitials, etc. The reduced specific volume of the oxides formed in the near-surface layer along with sub-surface nanometric voids and pores triggered by subtle ablation effects can render the material expansion, thus, elevating the HSFL-covered surface above the original surface plane, while leaving behind a chemically modified HAZ with a depth-extent of several tens of nanometers.

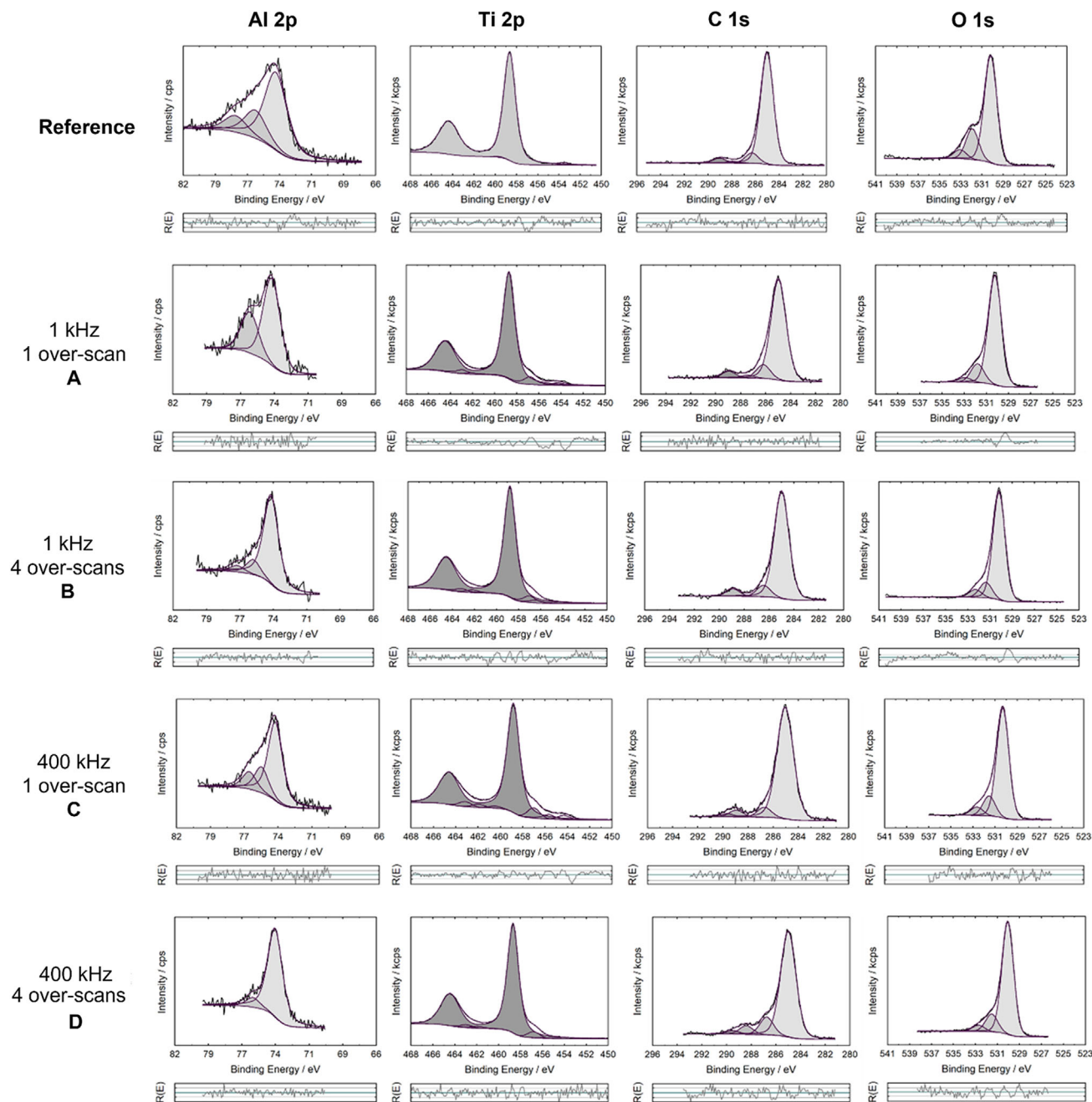


**Figure A1.** Deconvoluted high-resolution XPS spectra of the Al  $2p$ , Ti  $2p$ , C  $1s$ , and O  $1s$  transitions.  $R(E)$  visualizes the residual function of the least-squares-fits, i.e., the deviations between sum curves (purple) of all peaks and the experimental data (black data points).

## 4. Conclusions

High spatial frequency LIPSS with sub-100 nm spatial periods and modulation depths of several tens of nanometers were processed by an industrial ps-laser system on polished Ti-6Al-4V titanium alloy surfaces. A specific set of a peak fluence and a number of effective pulses ( $\phi_0 = 0.26 \text{ J cm}^{-2}$  and  $N_{\text{eff}} = 30$ ) was identified that allowed to homogeneously process HSFL-II at two different pulse repetition rates ( $f = 1 \text{ kHz}$  and  $f = 400 \text{ kHz}$ ) and for two different numbers of over-scans ( $\text{OS} = 1$  and  $\text{OS} = 4$ ) over  $2 \times 2 \text{ mm}^2$  sized surface areas in all  $f$ -OS-combinations. Topography measurements by AFM revealed that the HSFL spatial period  $\Lambda$  lies below 100 nm and is widely unaffected by the laser pulse repetition rate ( $f$ ), indicating that the thermal heat accumulation effects can be ruled out here even at  $f = 400 \text{ kHz}$ . In contrast, the spatial period  $\Lambda$  and the HSFL modulation depth  $h$  both moderately increase with OS. Simultaneously, the HSFL ridge length decreases with OS, while the degree of irregularity rises. However, note that among the latter experiments the total “dose of laser pulses per spot” ( $N_{\text{eff}} \times \text{OS}$ ) varies by a factor of four here.

Chemical analyses by ToF-SIMS, XPS, and HAXPES revealed that the ps-laser processing of HSFL-II on Ti-6Al-4V in air is

accompanied by the formation of laser-induced oxide layers with thicknesses exceeding 20 nm that consist mainly of  $\text{TiO}_2$ . The number of over-scans OS can affect a significant increase of the thickness of such superficial laser-induced oxide layers. Our multi-method chemical analyses by XPS/HAXPES/ToF-SIMS present consistent results of the laser-induced surface chemistry. Moreover, the direct comparison of the XPS and HAXPES data revealed the presence of surface-covering organic contaminants adsorbed from the ambient atmosphere. With an information depth 3 times larger than for XPS, HAXPES features superior analytical capabilities since any potential chemical reduction of the oxides by sputtering can be avoided here.

## Appendix A

The XPS and HAXPES data presented in Figure 5–7 as well as high-resolution spectra of the carbon C 1s transition were additionally deconvoluted into individual peaks. All spectra were processed with the program *Unifit* (version 2024).<sup>[38]</sup> A sum of Lorentzian and Gaussian was used as fit function in combination with a Shirley background. For each transition, a fixed peak shape was used among the samples. The Ti 2p peaks were fitted

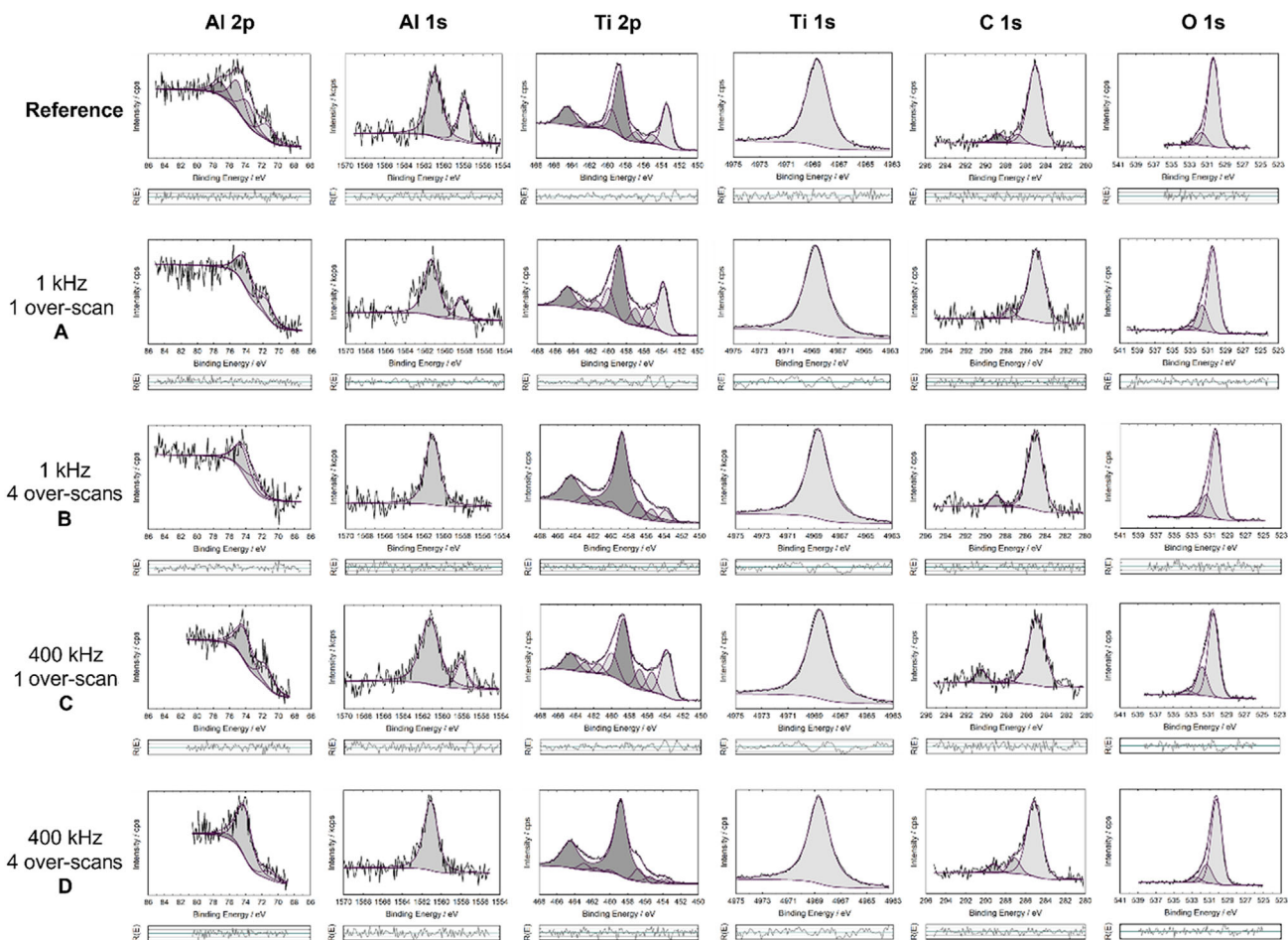


**Figure A2.** Deconvoluted high-resolution HAXPES spectra of the Al 2p, Al 2s, Ti 2p, Ti 1s, C 1s, and O 1s transitions.  $R(E)$  visualizes the residual function of the least-squares-fits, i.e., the deviations between sum curves (purple) of all peaks and the experimental data (black data points).

as doublets. The binding energies were referenced to the main C 1s peak with an electron binding energy of 285.0 eV. **Figure A1** shows the deconvoluted high-resolution XPS spectra, while **Figure A2** presents the corresponding HAXPES spectra.

## Acknowledgements

This work has received funding from the European Union's Horizon 2020 research and innovation program under grant agreement no. 951730 (LaserImplant). The authors would like to thank S. Benemann (BAM 6.1) for SEM characterization and S. Binkowski, C. Opitz, and K. Zieger (BAM 9.5) and M. Lagleder (BAM 6.1) for polishing the titanium samples. The help of M. Männ (BAM 6.1) with the VASE measurements for the sputter-rate calibration is acknowledged.

Open access funding enabled and organized by Projekt DEAL.

## Conflict of Interest

The authors declare no conflict of interest.

## Data Availability Statement

The data that support the findings of this study are available from the corresponding author upon reasonable request.

## Keywords

Ti–6Al–4V alloys, time-of-flight secondary ion mass spectrometry (ToF-SIMS), hard X-ray photoelectron spectroscopy (HAXPES), laser-induced periodic surface structures (LIPSS), nanostructures, ultrashort laser processing

Received: September 15, 2023

Revised: November 3, 2023

Published online:

- [1] H. M. van Driel, J. E. Sipe, J. F. Young, *Phys. Rev. Lett.* **1982**, *49*, 1955.
- [2] J. Bonse, S. Höhm, S. V. Kirner, A. Rosenfeld, J. Krüger, *IEEE J. Sel. Top. Quantum Electron.* **2017**, *23*, 9000615.
- [3] J. Bonse, S. Gräf, *Laser Photonics Rev.* **2020**, *14*, 2000215.
- [4] *Ultrafast Laser Nanostructuring — The Pursuit of Extreme Scales* (Eds: R. Stoian, J. Bonse), Springer Nature, Cham, Switzerland **2023**, <https://doi.org/10.1007/978-3-031-14752-4>.
- [5] A. Y. Vorobyev, C. Guo, *Laser Photon. Rev.* **2013**, *7*, 385.
- [6] J. Reif, in *Advances in the Application of Lasers in Materials Science* (Ed: P. Ossj), Springer, Cham, Switzerland **2018**, Ch. 3, [https://doi.org/10.1007/978-3-319-96845-2\\_3](https://doi.org/10.1007/978-3-319-96845-2_3).
- [7] C. Florian, S. V. Kirner, J. Krüger, J. Bonse, *J. Laser Appl.* **2020**, *32*, 022063.
- [8] S. Gräf, *Adv. Opt. Technol.* **2020**, *9*, 20190062.
- [9] E. Stratakis, J. Bonse, J. Heitz, J. Siegel, G. D. Tsiibidis, E. Skoulas, A. Papadopoulos, A. Mimidis, A. C. Joel, P. Comanns, J. Krüger, C. Florian, Y. Fuentes-Edfuf, J. Solis, W. Baumgartner, *Mater. Sci. Eng., R* **2020**, *141*, 100562.
- [10] S. Lifka, K. Harsányi, E. Baumgartner, L. Pichler, D. Baiko, K. Wasmuth, J. Heitz, M. Meyer, A.-C. Joel, J. Bonse, W. Baumgartner, *Beilstein J. Nanotechnol.* **2022**, *13*, 1268.
- [11] J. Heitz, E. Ahrenholz, D. Bäuerle, R. Sauerbrey, H. M. Phillips, *Appl. Phys. A* **1994**, *59*, 289.
- [12] J. Krüger, W. Kautek, *Appl. Surf. Sci.* **1996**, *96–98*, 430.
- [13] A. Rudenko, J.-P. Colombier, S. Höhm, A. Rosenfeld, J. Krüger, J. Bonse, T. E. Itina, *Sci. Rep.* **2017**, *7*, 12306.
- [14] N. Wu, Z. Wang, X. Wang, Y. Shimotsuma, M. Nishi, K. Miura, K. Hirao, *J. Ceram. Soc. Jpn.* **2011**, *119*, 898.
- [15] J. Bonse, S. Höhm, A. Rosenfeld, J. Krüger, *Appl. Phys. A* **2013**, *110*, 547.
- [16] X.-F. Li, C.-Y. Zhang, H. Li, Q.-F. Dai, S. Lan, S.-L. Tie, *Opt. Express* **2014**, *22*, 28086.
- [17] S. V. Kirner, T. Wirth, H. Sturm, J. Krüger, J. Bonse, *J. Appl. Phys.* **2017**, *122*, 104901.
- [18] X. Sedao, C. Maurice, F. Garrelie, J.-P. Colombier, S. Reynaud, R. Quey, F. Pigeon, *Appl. Phys. Lett.* **2014**, *104*, 171605.
- [19] P. Dominic, F. Bourquard, S. Reynaud, A. Weck, J.-P. Colombier, F. Garrelie, *Nanomaterials* **2021**, *11*, 1069.
- [20] A. Rudenko, A. Abou-Saleh, F. Pigeon, C. Mauclair, F. Garrelie, R. Stoian, J.-P. Colombier, *Acta Mater.* **2020**, *194*, 93.
- [21] H. Voss, X. Knigge, D. Knapic, M. Weise, M. Sahre, A. Hertwig, A. Sacco, A. Mario Rossi, J. Radnik, K. Müller, K. Wasmuth, W. Baumgartner, J. Krüger, J. Heitz, A.-W. Hassel, V.-D. Hodoroaba, J. Bonse, to be submitted to *Phys. Stat. Solidi A* **2023**.
- [22] S. V. Kirner, N. Slachciak, A. M. Elert, M. Griepentrog, D. Fischer, A. Hertwig, M. Sahre, I. Dörfel, H. Sturm, S. Pentzien, R. Koter, D. Spaltmann, J. Krüger, J. Bonse, *Appl. Phys. A* **2018**, *124*, 326.
- [23] C. Florian, R. Wonneberger, A. Undisz, S. V. Kirner, K. Wasmuth, D. Spaltmann, J. Krüger, J. Bonse, *Appl. Phys. A* **2020**, *126*, 266.
- [24] J. M. Liu, *Opt. Lett.* **1982**, *7*, 196.
- [25] J. Bonse, S. V. Kirner, J. Krüger, in *Handbook of Laser Micro- and Nano-Engineering* (Ed: K. Sugioka), Springer Nature, Cham, Switzerland **2021**, pp. 879–936, Ch. 23, [https://doi.org/10.1007/978-3-030-63647-0\\_17](https://doi.org/10.1007/978-3-030-63647-0_17). <https://imagej.nih.gov/ij/> (accessed: October 2023).
- [26] A. M. Richter, G. Buchberger, D. Stifter, J. Duchoslav, A. Hertwig, J. Bonse, J. Heitz, K. Schwibbert, *Nanomaterials* **2021**, *11*, 3000.
- [27] published under the GNU General Public License, Version 2, <http://gwyddion.net/> (accessed: October 2023).
- [28] E. O. Brigham, *The Fast Fourier Transform and its Applications*, Prentice-Hall, Englewood Cliffs, USA **1988**.
- [29] J. Bonse, H. Sturm, D. Schmidt, W. Kautek, *Appl. Phys. A* **2000**, *71*, 657.
- [30] J.-M. Savolainen, M. S. Christensen, P. Balling, *Phys. Rev. B* **2011**, *84*, 193410.
- [31] *CRC Handbook of Chemistry and Physics*, 76th ed. (Ed: D. R. Lide), CRC Press, Boca Raton, USA **1996**.
- [32] M. Prudent, D. Iabbaden, F. Bourquard, S. Reynaud, Y. Lefkir, A. Borroto, J.-F. Pierson, F. Garrelie, J.-P. Colombier, *Nano-Micro Lett.* **2022**, *14*, 103.
- [33] E. McCafferty, J. P. Wightman, *Appl. Surf. Sci.* **1999**, *143*, 92.
- [34] J. Bonse, S. Höhm, R. Koter, M. Hartelt, D. Spaltmann, S. Pentzien, A. Rosenfeld, J. Krüger, *Appl. Surf. Sci.* **2015**, *374*, 190.
- [35] Q. Zhu, H. Duan, B. Lin, Y. Zhu, Y. Hu, Y. Zhou, *Catal. Lett.* **2019**, *149*, 2636.
- [36] A. Rudenko, J.-P. Colombier, in *Ultrafast Laser Nanostructuring – The Pursuit of Extreme Scales* (Eds: R. Stoian, J. Bonse), Springer Nature, Cham, Switzerland **2023**, pp. 209–255, Ch. 5, [https://doi.org/10.1007/978-3-031-14752-4\\_5](https://doi.org/10.1007/978-3-031-14752-4_5).
- [37] Proprietary Software, <https://www.unifit-software.de> (accessed: October 2023).